ROYAL SOCIETY
OF CHEMISTRY

PAPER

Check for updates

Selective synthesis of visible light active γ-bismuth molybdate nanoparticles for efficient photocatalytic degradation of methylene blue, reduction of 4-nitrophenol, and antimicrobial activity†

B. Lavakusa,[*a] Dharmaoth Rama Devi,[b] Neway Belachew [ID] [*c] and K. Basavaiah [ID] [*d]

In this study, we have reported selective synthesis of bismuth molybdate (γ-$Bi_2M_2O_6$) nanoparticles (NPs) under different pH conditions for photocatalytic degradation of methylene blue (MB), reduction of 4-nitrophenol (4-NP) to 4-aminophenol (4-AP) and antimicrobial activities. The synthesis of pure phase γ-$Bi_2M_2O_6$ at pH = 3 was confirmed by X-ray diffraction (XRD) and Raman analysis. A single hexagonal morphology was obtained at pH = 3 which shows the formation of the pure phase γ-$Bi_2M_2O_6$ NPs. The mixed morphologies (hexagonal and spherical) were observed at different pH values other than pH = 3. The bandgap energy of all the synthesized $Bi_2M_2O_6$ NPs is found in the visible region (2.48–2.59 eV). The photocatalytic activity of bismuth molybdate (BM) NPs was examined by the degradation of MB under visible light irradiation. Results show that 95.44% degradation efficiency was achieved by pure γ-$Bi_2M_2O_6$ NPs compared to mixed phases (γ-$Bi_2M_2O_6$, α-$Bi_2M_2O_6$ and β-$Bi_2M_2O_6$) synthesized at pH = 1.5 and 5. Moreover, the degradation efficiency of γ-$Bi_2M_2O_6$ was enhanced to 98.89% by the addition of H_2O_2. The effective catalytic activity of γ-$Bi_2M_2O_6$ was observed during the reduction of 4-NP to 4-AP by $NaBH_4$. Potential antibacterial and antifungal activity of γ-$Bi_2M_2O_6$ was observed, which gives a basis for further study in the development of antibiotics.

1. Introduction

During the past few decades, there has been observed huge contamination of water bodies by organic pollutants that are released from industrial and microorganisms such as bacteria, and fungi. As a consequence, millions of people, especially in developing countries, have been confronted with waterborne diseases such as diarrhea, vomiting, and cholera.[1] Some of the compounds are carcinogenic and mutagenic in nature for aquatic life. This shows that there is a need to treat polluted water before discharging to the environment. To date, numerous water purification methods such as adsorption, advanced oxidation process (AOPs), coagulation, and membrane separation have been employed for the removal of contaminants.[2,3] Among them, AOPs show great attention to removing microorganisms and dyes from contaminated water.[4]

AOP based on photocatalytic degradation of organic pollutants and destruction of microbes has taken both research and marketing interests.[5–7] Titanium dioxide (TiO_2) is the most popular semiconductor used in heterogeneous photocatalysis due to high stability, chemical inertness, low cost, and non-toxicity.[6,8,9] However, the bandgap of TiO_2 (3.2 eV) is not suitable for the harvesting of light in the visible region, the most abundant component of solar radiation reaches on the earth's surface.[9–11] To improve the photocatalysis efficiency under visible light irradiation, many methods have attempted to decrease the high bandgap energy photocatalyst.[12–14] Likewise, development of a series of new visible-light photocatalysts were designed and prepared with the decreased bandgap energy, such as $InVO_4$,[15] $Sr_2Nb_2O_7$,[16] $Sr_2Ta_2O_7$,[17] and bismuth oxides, like $BiOBr$,[18] $Bi_{12}TiO_{19}$,[19] $BiVO_4$,[20] Bi_2WO_6,[21] Bi_2O_3 (ref. 22) and Bi_2MoO_6 (ref. 23) as to make maximize the utilization of solar energy. Among them, bismuth molybdates, as novel semiconductor photocatalysts, have been determined to have an excellent performance in solar-light-mediated systems, showing great potential in applications such as water splitting and environmental purification.[24] Bismuth oxides exhibit both

[a] VKR College, Buddhavaram, Gannavaram-521101, India. E-mail: lavakusa99@gmail.com

[b] A. U. College of Pharmaceutical Sciences, Andhra University, Visakhapatnam-530003, India

[c] Department of Chemistry, Debre Berhan University, Debre Berhan, Ethiopia. E-mail: neway.du@gmail.com/neway@dbu.edu.et

[d] Department of Inorganic and Analytical Chemistry, Andhra University, Visakhapatnam, India-53000. E-mail: klbasu@gmail.com

a high oxide ion conductivity and an electrocatalytic activity for the interconversion of molecular O_2 and ionic O_2^- at low temperature (300–500 °C) and thus have an important potential for oxygen generation.[24,25] The general chemical formula of bismuth molybdate is $Bi_2O_3 \cdot nMoO_3$, where $n = 3$, 2 or 1 which are corresponding to α ($Bi_2Mo_3O_{12}$), β ($Bi_2Mo_2O_9$), and γ (Bi_2MoO_6) phases respectively. Of these, the γ-Bi_2MoO_6 phase has excellent intrinsic physical, chemical properties[26,27] and shows numerous applications in various fields. But, selective synthesis of γ-Bi_2MoO_6 NPs with desired morphology using a facile approach is yet a challenge. Besides, there is limited or no report on the catalytic and antimicrobial activity of γ-Bi_2MoO_6 NPs.

Hence, in this study, we have reported a facile and selective synthesis of γ-Bi_2MoO_6 NPs at different pH of the solution. The formation of the desired phase, structure, and morphology was investigated by XRD, Raman spectroscopy, FTIR, FESEM-EDS, and TEM-SAED analysis. The photocatalytic activity of Bi_2MoO_6 NPs was evaluated by the degradation of MB at visible light irradiation. The catalytic efficiency and antimicrobial of Bi_2MoO_6 NPs were also investigated.

2. Experimental

2.1. Materials

Bismuth nitrate ($Bi(NO_3)_3 \cdot 5H_2O$), nitric acid (HNO_3 78%), ammonium molybdate (($NH_4)_6Mo_7O_{24} \cdot 4H_2O$), ammonium hydroxide ($NH_4OH$), methylene blue ($C_{16}H_{18}ClN_3S$), hydrogen peroxide ($H_2O_2$), DMSO ($C_2H_6OS$), ciprofloxacin ($C_{17}H_{18}FN_3O_3$), clotrimazole ($C_{22}H_{17}ClN_2$), and Mueller-Hinton agar powder were received from Merck, India and used without further purification. Microorganisms such as *Escherichia coli* (Gram-negative bacteria), *Staphylococcus aureus* (Gram-positive bacteria), and *Aspergillus niger* (fungus) were used to investigate the antimicrobial activities.

2.2. Synthesis of bismuth molybdate under various pH conditions

A facile co-precipitation method was used to synthesize bismuth molybdate nanoparticle under different pH conditions. In particular, 4.75 g of $Bi(NO_3)_3 \cdot 5H_2O$ (0.49 M) was dissolved in 20 mL of dilute HNO_3 (1.5 M). The solution was then added dropwise into the aqueous solution containing 0.035 M of ($NH_4)_6Mo_7O_{24} \cdot 4H_2O$ (0.86 g/20 mL) under vigorous stirring. The pH of the mixed solution was precisely adjusted at 1.5, 3.0, and 5.0. The reaction of the solution continuously stirred at room temperature for 8 h and the obtained precipitate was filtered, dried, and then it was calcined at 475 °C for 5 h to yield the bismuth molybdate NPs. Samples prepared at pH 1.5, 3, and 5 were labeled as BM1, BM2, and BM3, respectively.

2.3. Characterization of the prepared catalyst

The crystalline structure of the synthesized bismuth molybdate NPs was investigated by powder X-ray diffraction (XRD, PAN-alytical, X'Pert pro, Netherland) with Cu Kα (1.54218 Å) radiation in the scan rate of 0.050/0.05 s. Fourier transform infrared

spectra of the sample were recorded on FTIR spectrometer (IR Prestige 21, Shimadzu, Pvt Ltd, Japan) using conventional potassium bromide (KBr) pellets within a wavenumber range 5000–500 cm^{-1}. Raman spectra recorded using Raman Spectrometer (BWTEK MiniRam BTR-111Miniature) with the Raman shift range 200–1200 cm^{-1}. The size and morphology of the product were obtained from Field Emission scanning electron microscope (FESEM, CARL Zeiss Germany, FESEM Ultra55, Gemini column, 1 nm Resolution, the detector is In-lens SE) and Energy dispersive X-ray analysis (EDX, Oxford company, model 20 nm X Ma). Transmission electron microscopy (FEI Tecnai G2 F20 S-Twin TEM). UV-vis diffuse reflectance spectra of the sample were obtained in the range of 300–800 nm using a UV-vis spectrophotometer (UV2600, Shimadzu, Japan) with barium sulphate ($BaSO_4$) was used as a reflectance standard. The photocatalytic activity was monitored using a UV-visible spectrophotometer (UV 2700, Shimadzu, Japan) over the range of 200–800 nm.

2.4. Photocatalytic activity of catalyst under visible light irradiation

The photocatalytic activities were evaluated by the decomposition of methylene blue (MB) in aqueous solution at ambient temperature. The chemical composition of the simulated wastewater was derived from the guidelines established by the Indian water standard IS 10500 (2012). The reaction was conducted in a cylindrical quartz reactor (100 mL) with a water circulation facility. A 400 W Hg-X lamp was used as the light source to provide the simulated solar light. The experiments were performed at room temperature. The photocatalysts (0.05 g) were added into 50 mL of organic dye pollutant (5 mg L^{-1}) solution and the suspension was magnetically stirred for 30 minutes to establish adsorption–desorption equilibrium between the photocatalyst surface and MB. At every 30 minutes time intervals, a 3 mL of solution was collected and separated by centrifugation at 2600 rpm for 5 minutes and then analyzed using a UV-vis spectrophotometer. The photocatalytic degradation process was performed by all the synthesized catalysts (BM1, BM2, BM3). The concentration of MB dye in the solution is determined by monitoring the absorption at 664 nm. Decolorization efficiency (%) was calculated using eqn (1).

$$\text{Decolorization efficiency } (\%) = (C_0 - C)/C_0 \times 100 \qquad (1)$$

where 'C_0' is the initial concentration of MB and 'C' is the concentration of MB after light irradiation.

2.5. ˙OH radical formation probed by PL spectra

50 mg of photocatalyst was added to 100 mL of terephthalic acid (TPA) solution (0.25 mmol L^{-1} in 1 mmol L^{-1} NaOH solution). The solution is stirred for 30 min in dark followed by irradiation using 400 W of HgX lamp for 45 min. The reacted solution was centrifuged to get clear solution for photoluminescence (PL) measurements in a fluorescence spectrofluorometer (FlouroMax-4) at the excitation wavelength of 315 nm.

2.6. Catalytic reduction of 4-nitrophenol

The prepared bismuth molybdate was evaluated as catalysts for the reduction reaction of 4-nitrophenol (4-NP) to 4-amino-phenol (4-AP) using sodium tetrahydroborate (NaBH$_4$) as a reducing agent. The catalytic tests were conducted as follows: 40 mL of a sodium tetrahydroborate NaBH$_4$ solution (8×10^{-4} M) was added under continuous stirring to 10 mL of a 4-NP solution at 5 mg L^{-1}. Then, an intense yellow color appeared because of the formation of a 4-nitrophenolate anion in the solution. To the resulting solution, 5 mg of the bismuth molybdenum catalyst added. The catalytic reduction was monitored measuring the absorbance at the $\lambda_{max} = 400$ nm of 4-nitrophenolate ion.

2.7. Microbial growth inhibition

The antimicrobial activities of synthesized γ-Bi$_2$MoO$_6$ NPs were investigated against Gram-negative bacteria (*Escherichia coli*), Gram-positive bacteria (*Staphylococcus aureus*) bacteria, and fungus (*Aspergillus niger*).[28] The detailed procedures of antimicrobial activity are presented in SI 1 and SI 2.†

3. Results and discussion

3.1. Characterization analysis

The crystalline structures of the synthesized samples were examined by powder XRD. Fig. 1 shows the XRD patterns of bismuth molybdate NPs obtained at different pH values. It is well known that the initial pH values of the precursor solutions play an important role in the formation of different phases of the Aurivillius oxide, Bi$_2$MoO$_6$ (BM) structure. Fig. 1 shows the well-defined diffraction peak at $2\theta = 28.43°$ and $32.76°$ which are due to the diffraction pattern of γ-Bi$_2$MoO$_6$, a small intensity at $2\theta = 27.94°$, and 32.020 which are matching to the diffraction pattern of β-Bi$_2$Mo$_2$O$_9$, and a very small intensity at $2\theta = 30.05°$ is indexed to α-Bi$_2$Mo$_3$O$_{12}$·29Bi$_2$MoO$_6$ synthesized at pH = 1.5 (BM1) shows the formation of multiple phases of bismuth molybdate (γ-Bi$_2$MoO$_6$, β-Bi$_2$Mo$_2$O$_9$, α-Bi$_2$Mo$_3$O$_{12}$). Similarly,

Bi$_2$MoO$_6$ obtained from pH = 5.0 (BM3) shows the formation of two phases of bismuth molybdate (γ-Bi$_2$MoO$_6$, β-Bi$_2$Mo$_2$O$_9$). Whereas, only one phase of bismuth molybdate (γ-Bi$_2$MoO$_6$) was obtained at pH = 3.0 (BM2). The distinct diffraction peaks of different samples at 11.06°, 23.69°, 28.02°, 28.43°, 32.02°, 32.76°, 33.31°, 36.20°, 46.86°, 47.33° correspond to the (020), (131), (111), (131), (200), (002), (060), (151), (260) and (202) crystal planes of Bi$_2$MoO$_6$ (JCPDS: 21-0102 and 84-0787), respectively. The average crystallite size was calculated from the line broadening of the diffraction peaks using the Scherrer eqn (2).

$$L = 0.9\lambda/(\beta \cos \theta) \qquad (2)$$

Where L is the crystalline size, β is the line width of full width half maximum value (FWHM) and λ is the wavelength of X-rays. The average crystalline size of γ-Bi$_2$MoO$_6$ was found to be 8.20 nm with a lattice strain 0.0156. Moreover, the lattice parameters of γ-Bi$_2$MoO$_6$ were determined using eqn (3) and (4).[30] The lattice parameters of the hexagonal γ-Bi$_2$MoO$_6$ that obtained at pH = 3 are $a = 5.1896$ Å, $b = 11.7107$ Å, and $c = 5.1896$ Å and total volume of the unit cell = $V = 272.91$.

$$1/d^2 = 4/3((h^2 + k^2 + hk)/a^2) + l^2/c^2 \qquad (3)$$

where the h, k, and l are Miller's indices. a, b, and c are lattice cell parameters. 'd' is interplanar distance.

$$\text{Total volume of unit cell volume } (V) = 0.866a^2b \qquad (4)$$

Fig. 2(a) shows the Raman spectra of bismuth molybdate NPs synthesized at different pH conditions. BM1 sample shows the vibration bands at 282 cm^{-1}, 325 cm^{-1}, 352 cm^{-1}, 401 cm^{-1}, 715 cm^{-1}, 795 cm^{-1}, 849 cm^{-1}, and 885 cm^{-1}. For BM2 vibration band at 885 cm^{-1} is not observed, while it is observed in small intensity in BM3 compared to BM1. These spectra reveal that the high degree of purity of the γ-Bi$_2$MoO$_6$ (BM2) phase because the extraneous Raman band (885 cm^{-1}) is not observed, unlike others. This implies that the formation of the desired phase of Bi$_2$MoO$_6$, γ-Bi$_2$MoO$_6$, is strongly the pH of the solution, and therefore, the pH = 3.0 is optimum for the formation of γ-phase (γ-Bi$_2$MoO$_6$). The vibrational bands 849 cm^{-1}, and 795 cm^{-1} peaks can be ascribed to the stretching modes of Mo–O bonds, and vibrational band 715 cm^{-1} peak can
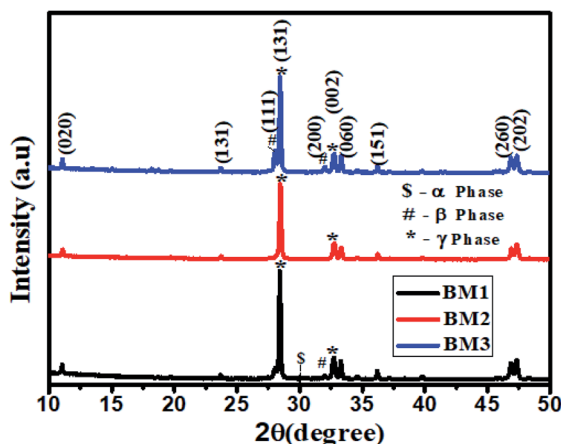

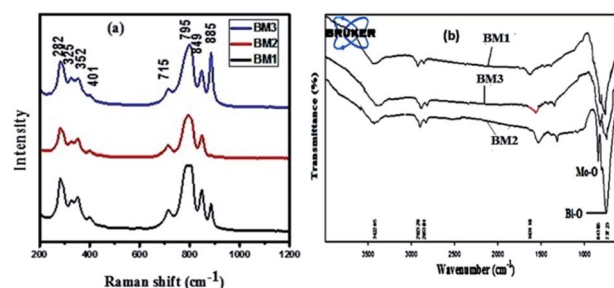**Fig. 1** The XRD patterns of bismuth molybdate synthesised from at different pH.

Fig. 2 (a) Raman spectra (b) FTIR spectra of bismuth molybdate NPs.

be the stretching modes of Bi–O/Bi–O–Mo stretching observed.[29] The FT-IR spectrum of bismuth molybdate NPs synthesized at different pH conditions are presented in Fig. 2(b). The main absorption bands at 736 cm^{-1}, 798 cm^{-1}, 843 cm^{-1} are mainly related to Bi–O and Mo–O stretching modes.[31] Generally the absorption bands between 400–950 cm^{-1} range described to Bi–O and Mo–O stretching and Mo–O–Mo bridging stretching modes.[31–33] Moreover, the bond length of Mo–O/Bi–O–Mo can be predicted from the Raman stretching frequencies using eqn (5).[34]

$$R_{\text{Mo–O}} = 0.482\ 39 \ln(32\ 895/u) \tag{5}$$

where u is the Raman stretching frequency in wavenumbers and R is the metal–oxygen bond length in angstroms.

The Pauling bond strengths of metal–oxygen bonds also referred to as bond orders or bond valences, are useful for reasonably predict the metal oxide structures.[34] The Pauling bond strength reflects the relative distribution of available valence electrons throughout the covalent bonds of a metal oxide species, and eqn (6) relating Mo–O bond lengths 'R' to their Pauling bond strength 's'.[34]

$$s = (R/1.882)^{-0.6} \tag{6}$$

By combining eqn (5) and (6), a relation between the Pauling strength of a Mo–O bond length in valence units and its Raman stretching frequency in wavenumbers is expressed as, eqn (7).[35,36] The predicted bond length of Mo–O in Å (Table 1) is found in agreement with reported literature.[37]

$$S_{\text{Mo–O}} = \{0.256 \ln(32895/u)\}^{-6.0} \tag{7}$$

The morphologies and structure of the bismuth molybdate (BM1, BM2, BM3) NPs were investigated using SEM and TEM analysis. Fig. 3(a and c) shows the FE-SEM images of bismuth molybdate that synthesized at pH 1.5 (BM1), and 5.0 (BM3), respectively. The image clearly shows a smooth surface with mixed morphology including spherical shapes and some hexagonal structure. It reveals to pH conditions of 1.5 and 5.0, which contained impure α and β phases result in mixed morphology. Instead, Fig. 3(b) shows observed the only hexagonal structure of synthesized NPs due to the formation of pure phase γ-Bi$_2$MoO$_6$ NPs at pH = 3.0 with the particle size range of
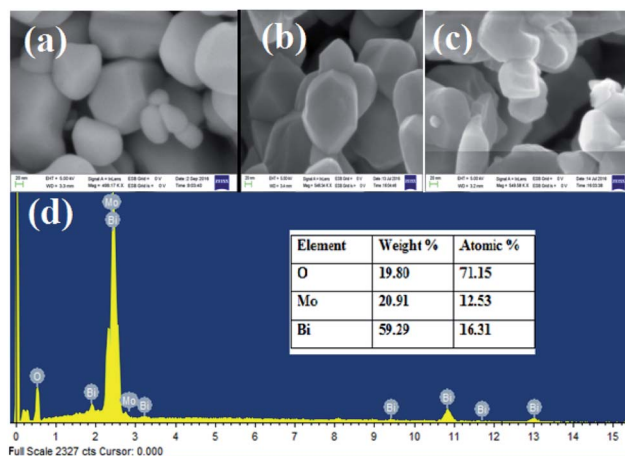

Fig. 3 FE-SEM images of bismuth molybdate synthesised at (a) pH = 1.5, (b) pH = 3, (c) pH = 5 values, and (d) EDX analysis of BM2 nanoparticle.

47–90 nm. Fig. 3(d) shows the EDX analysis for elemental composition and purity of synthesized γ-Bi$_2$MoO$_6$ NPs, and the result shows the presence of elements like Bi, Mo, and O.

TEM images of the bismuth molybdate sample obtained at different pH values are shown in Fig. 4(a–c). Under acidic conditions (pH 1.5, pH 3.0, pH 5.0), all of the bismuth molybdate NPs exhibit hexagonal structures. Fig. 4(e) shows the SAED image of γ-Bi$_2$MoO$_6$ NPs and interlayer spacings of 0.274 nm, 0.275 nm and 0.39 nm for the (002), (200) and (111) diffraction, respectively. Fig. 4(f) shows the particle size distribution histogram of γ-Bi$_2$MoO$_6$ NPs obtained from Fig. 4(d) image and it was predicted to be 6 nm.

As shown in Fig. 5, the three samples show the photoabsorption properties from the UV to the visible light region. The steep absorption edges are observed for all samples, indicate the absorption is due to the intrinsic transition rather than a transition from impurity levels.[37] UV-DRS spectra of synthesized bismuth molybdate NPs, sample exhibited absorption

Table 1 The calculated bond length of Mo–O bond of γ-Bi$_2$MoO$_6$

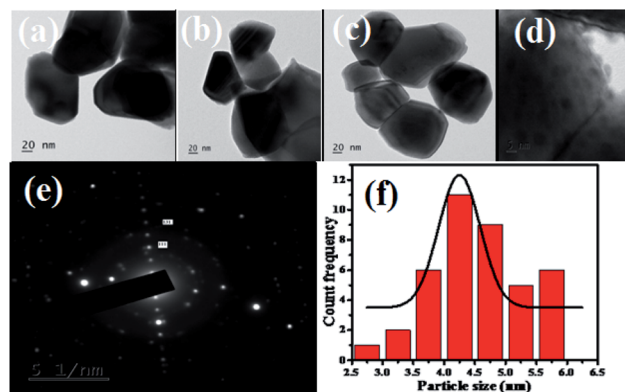| Band position (frequency – u) cm^{-1}	$R_{\text{Mo–O}}$ species bond length (Å)	$S_{\text{Mo–O}}$ species bond length (Å)
282	2.29	2.10
325	2.22	2.08
352	2.18	2.07
401	2.12	2.05
715	1.84	1.99
795	1.79	1.98
849	1.76	1.97
885	1.74	1.97

Fig. 4 (a–c) TEM images of bismuth molybdate prepared at different pH values in 20 nm scale range, (d). BM2 at 6 nm range scale, (e). SAED analysis of BM2 nanoparticle, and (f). Particle size distribution histogram of BM2 NPs.
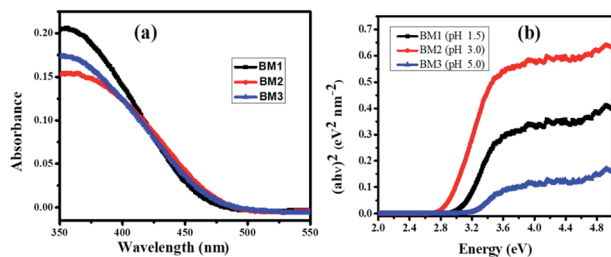
Fig. 5 (a) UV-vis diffuse reflectance spectra and (b) it's corresponding Tauc's plot of bismuthmolybdate NPs.

edge at 479 nm, 499 nm, and 486 nm for BM1, BM2, and BM3 NPs, respectively. The calculated bandgap energy, from eqn (8), for the BM1, BM2, and BM3 NPs are found to be 2.59 eV, 2.48 eV, and 2.55 eV respectively. Generally, narrow bandgap semiconductors materials are suggested for efficient charge separation and efficient absorption in the visible light region. As can be seen, γ-Bi_2MoO_6 samples exhibit a shift of the absorption edge to longer wavelengths, in the visible light region, indicating that the sample has the potential for photocatalytic decomposition of organic contaminants under visible-light irradiation.

$$Bandgap\ energy\ (E_g) = h \times c/l \qquad (8)$$

where E_g, h, c, l are bandgap energy, plank constant, the speed of light, cut off wavelength respectively.

3.2. Photocatalytic degradation of methylene blue analysis

The photocatalytic activity of the synthesized BM (BM1, BM2, BM3) NPs was investigated by using MB as a model water pollutant. Fig. 6(a) depicts the UV-vis absorption spectra of MB at different durations under visible light irradiation in the absence of the photocatalyst. The absorption peak of MB slowly decreases and reached a maximum degradation (7.62%) at 120 min. This ascribes the needs of photocatalyst for a successful degradation of MB. Fig. 6(b–d) show the absorption spectra of MB dye solution irradiated by the visible light in the presence of BM1, BM2, and BM3 NPs. As it is shown in Fig. 6(b–d), BM2 shows greater degradation efficiency than both BM1 and BM3 which is due to the high efficiency of the pure phase Bi_2MoO_6 for separating the photogenerated carriers (e^- and h^+). Fig. 6(e) presents the UV-vis spectra of MB irradiated by the visible light in the presence of BM2 + H_2O_2, the peak intensity of MB abruptly vanished close to zero absorbance at 664 nm. This indicates the synergy of the BM catalyst and H_2O_2. As shown in Fig. 6(f), the rate of degradation of MB increases with the combination of the catalyst and H_2O_2. It was obtained 87.87%, 95.44%, 91.28% and 98.89% degradation efficiency for BM1, BM2, BM3, and BM2 + H_2O_2, respectively at the end of 120 min. The BM2 catalyst still shows a better efficiency than a yardstick photocatalysts such as ZnO and TiO_2 NPs.[14]

    The first-order was used to investigate the kinetics of photocatalytic degradation of MB by BM1, BM2, BM3, and BM2 + H_2O_2 (Fig. 7). The kinetics plot illustrates experimental data of
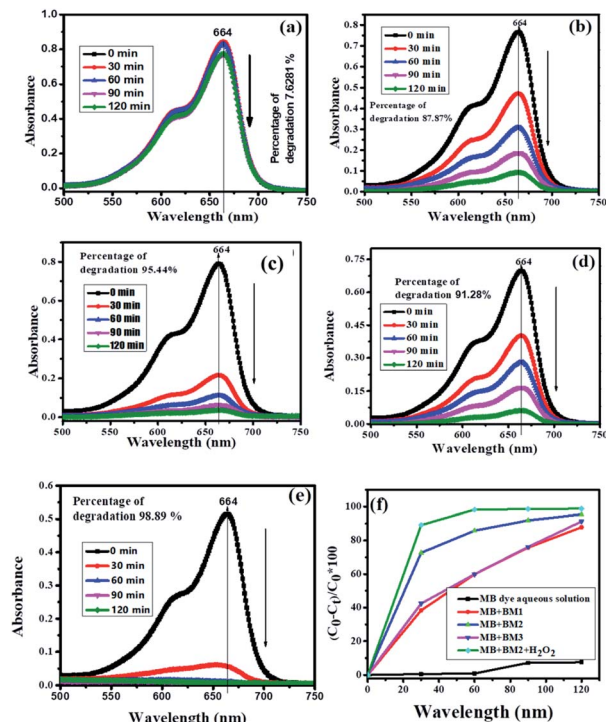

Fig. 6 Absorbance spectra of UV-visible for degradation of MB dye under visible light irradiation (a) MB dye aqueous solution (b) MB dye with BM1 (c) MB dye with BM2 (d) MB dye with BM3 (e) MB dye with BM2 + H_2O_2 (f) photocatalytic comparison between MB dye aqueous solution, BM1, BM2, BM3, and BM2 + H_2O_2 under visible light irradiation as a function of time 't' verses % of degradation.

the MB degradation rate by BM1, BM2, and BM3 shows the good fitting the first-order kinetic model. The steepest slope of BM2 shows the reaction is faster than BM1 and BM3. The deviation of experimental data from the first-order kinetics model was observed in the case of BM2 + H_2O_2. This infers that the kinetics of MB degradation by BM2 + H_2O_2 matrix do not explained sufficiently by first order model.
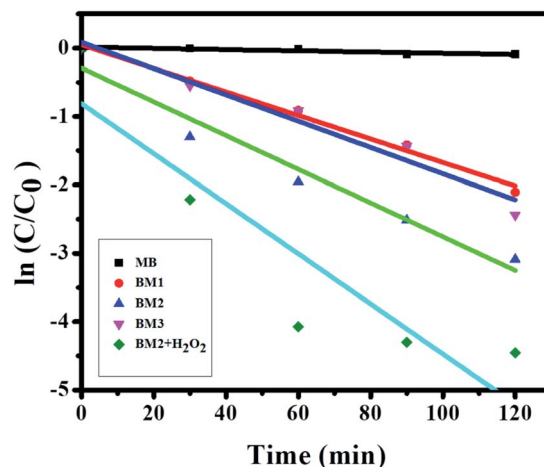

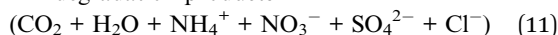Fig. 7 First order kinetic MB degradation by the bismuth molybdate.

The plausible degradation of MB initial proceeds *via* activation of Bi_2MoO_6 (BM) by light (hu) or hydrogen peroxide (H_2O_2) which produces electron–hole pairs ($h^+/e-$). These reactive species play a prominent role in the mineralization of organic compounds. The general mechanism for the degradation of MB is presented in eqn (9–11).

$$BM + hv \rightarrow h^+ + e^- \quad (9)$$

$$OH^- + h^+ \rightarrow {}^\cdot OH \quad (10)$$
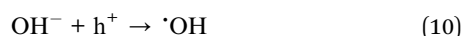
MB + ${}^\cdot$OH → degradation products
$$(CO_2 + H_2O + NH_4^+ + NO_3^- + SO_4^{2-} + Cl^-) \quad (11)$$

The hydroxyl radical which comes from the oxidation of adsorbed water or adsorbed OH^- is the primary oxidant for the degradation of MB. The final products of the photocatalytic degradation of MB result in the formation of CO_2, H_2O, and others.[38,39]

The formation of ${}^\cdot$OH radical was probed by photoluminescence (PL) spectroscopy.[36] Fig. 8 shows the PL spectra recorded after visible light irradiation for 90 min. In particular, the BM2 photocatalyst was dispersed in a terephthalic acid (TPA) solution and irradiated by visible light. Then, the photocatalyst releases ${}^\cdot$OH radical that readily reacts with TPA to form 2-hydroxyterephthalic acid, which emits a blue emission signal at approximately 432 nm. The formation of the strong intensity of the emission peak at 432 nm reflects the amounts of ${}^\cdot$OH radical produced during photoirradiation. Fig. 8 reveals the photoluminescence spectra of TPA solutions in the presence of γ-Bi_2MoO_6 (BM2) under visible light irradiation. The formation of a strong PL peak at 432 nm confirms the formation ${}^\cdot$OH reacts with TPA under visible light irradiation in the presence of γ-Bi_2MoO_6, which in turn it shows that the catalyst is visible light active.

3.3. Reduction of 4-nitrophenol (4-NP) into 4-aminophenol (4-AP_)

The reduction reaction of 4-NP with $NaBH_4$ was investigated to test the catalytic efficiency of BM2. Fig. 9 shows the catalytic activity of BM2 for the reduction 4-NP to 4-AP in the presence of $NaBH_4$ as a reducing agent. Without adding the catalyst, the dark yellow color of the 4-NP solution (5 ppm) did not bring color change within a period of 24 h (Fig. S1†). However, after the addition of the BM2, the solution becomes colorless in few minutes. The absorption peak of 4-NP located at 400 nm disappear and simultaneously new peaks situated at 300 nm is formed, which indicates the formation of 4-AP. This shows that BM2 is a promising catalyst for the reduction of 4-NP. The plausible reduction of mechanim of 4-NP using BM is proposed as shown in eqn (12) and (13). The homolytic dissociation of the BH_4^- bond (H^+ and BH_3^-), which results in the formation of reactive species (Bi_2MoO_6)–H and (Bi_2MoO_6)–BH_3, eqn (12). Then 4-AP formed from the activated proton (H^+) reacts 4-NP, eqn (13) and (14).[40]

$$2BiMoO_6 + BH_4- \rightarrow (BiMoO_6)-H + (BiMoO_6)-BH_3^- \quad (12)$$

$$6(BiMoO_6)-H + NP \rightarrow AP + 6BiMoO_6 + 6H^+ \quad (13)$$

$$6(BiMoO_6)-BH_3^- + NP \rightarrow AP + 6BiMoO_6 + 6BH_3 \quad (14)$$

3.4. Antimicrobial activity of BM2 NPs

The anti-microbial activities of BM2 NPs were explored against anti-bacterial strain Gram-positive (*staphylococcus aureus*), Gram-negative bacteria (*Escherichia coli*), and anti-fungal representative (*Aspergillus niger*). As shown in Fig. 10, BM2 NPs show the potential for the inhibitions for both bacterial and fungal growth. A large zone of inhibition was found in fungal compared with both bacterial strains. Table S1† shows BM2 NPs exhibited a maximum zone of inhibition against fungus (*Aspergillus niger*) than against bacteria. It seems that fungus (*Aspergillus niger*) is more sensitive than bacteria towards BM2.
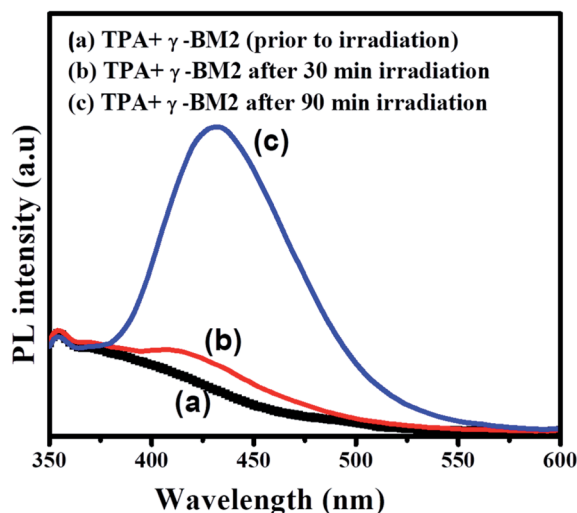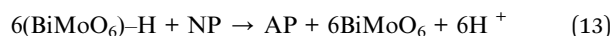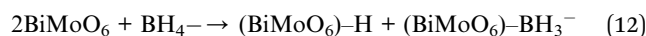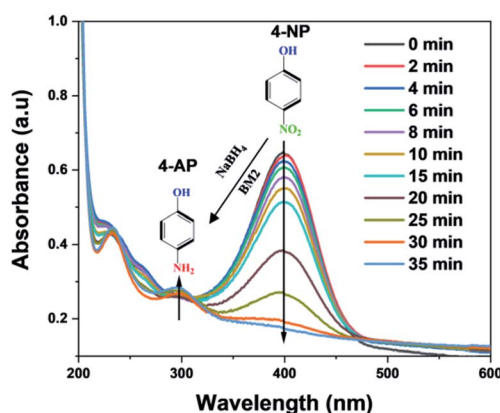

Fig. 8 Photoluminescence spectra of TPA solutions containing BM2 in presence of visible light irradiation (TPA = 0.25 M 100 mL, BM2 = 50 mg).

Fig. 9 UV-visible spectra of the reduction reaction of 4-nitrophenol in the presence of $NaBH_4$ with BM2 nanoparticles.
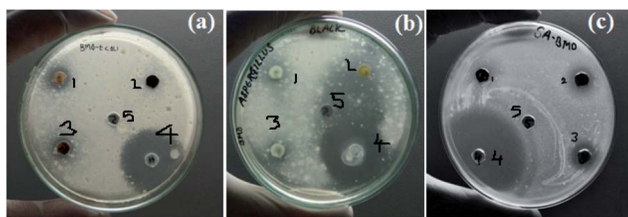
Fig. 10 The images of antimicrobial assay of BM2 nanoparticles (a) *E. coli*, (b) *A. niger*, and (c) *S. aureus* {1,2, and 3 amount of BM NP's 10 mg mL^{-1}, 5 mg mL^{-1}, and 2.5 mg mL^{-1} respectively, 4-standard (antibiotic or antifungal), 5-DMSO (solvent)}.

Due to the strong bioactivity BM2 NPs especially for fungus, this work can be a basis for further studies in the development of efficient antibiotics against fungal infections.

4. Conclusions

In conclusion, a facile coprecipitation method was used for selective synthesis of γ-Bi$_2$MoO$_6$ at pH = 3. The pH of the solution was found to be crucial for the synthesis of a pure phase of γ-Bi$_2$MoO$_6$ with a single hexagonal morphology. The diffraction and Raman analysis confirm the formation of pure phase γ-Bi$_2$MoO$_6$ NPs with a single morphology. All the synthesized BM NPs show an absorption edge in the visible region. The γ-Bi$_2$MoO$_6$ NPs show interesting photocatalytic degradation efficiency for MB under visible light irradiation. It was achieved 95.44% degradation of MB (5 mg L^{-1}) by BM2 (γ-Bi$_2$MoO$_6$ NPs) than 87.87% for BM1, and 91.28% for BM3. The maximum degradation (98.89%) of MB was obtained by γ-Bi$_2$MoO$_6$ NPs in the presence of H$_2$O$_2$ which is due to hydrogen peroxide is a good initiator to start the free radical formation. The catalytic role of γ-Bi$_2$MoO$_6$ NPs was observed by the fast reduction of 4-NP to 4-AP. The γ-Bi$_2$MoO$_6$ NPs had shown a promising for antibacterial activity against Gram-positive (*staphylococcus aureus*), Gram-negative bacteria (*Escherichia coli*), and anti-fungal (*Aspergillus niger*).

Conflicts of interest

There are no conflicts to declare.

Acknowledgements

References

1 I. Ali and H. Y. Aboul-Enein, *Chiral Pollutants: Distribution, Toxicity and Analysis by Chromatography and Capillary Electrophoresis*, John Wiley & Sons, 2005.

2 N. Belachew, D. Rama Devi and K. Basavaiah, *J. Mol. Liq.*, 2016, **224**, 713–720.

3 S. M. Botsa, D. Ramadevi and K. Basavaiah, *J. Nanosci. Tech.*, 2018, **4**(5), 467–470.

4 P. R. Gogate and A. B. Pandit, *Adv. Environ. Res.*, 2004, **8**, 501–551.

5 X. Chen, S. Shen, L. Guo and S. S. Mao, *Chem. Rev.*, 2010, **110**, 6503–6570.

6 T. L. Thompson and J. T. Yates Jr, *Chem. Rev.*, 2006, **106**, 4428–4453.

7 M. H. Kahsay, A. Tadesse, D. RamaDevi, N. Belachew and K. Basavaiah, *RSC Adv.*, 2019, **9**, 36967–36981.

8 D. P. Macwan, P. N. Dave and S. Chaturvedi, *J. Mater. Sci.*, 2011, **46**, 3669–3686.

9 T. Sugimoto and X. Zhou, *J. Colloid Interface Sci.*, 2002, **252**, 347–353.

10 J. L. Gole, J. D. Stout, C. Burda, Y. Lou and X. Chen, *J. Phys. Chem. B*, 2004, **108**, 1230–1240.

11 M. Ni, M. K. H. Leung, D. Y. C. Leung and K. Sumathy, *Renewable Sustainable Energy Rev.*, 2007, **11**, 401–425.

12 M. Iwasaki, M. Hara, H. Kawada, H. Tada and S. Ito, *J. Colloid Interface Sci.*, 2000, **224**, 202–204.

13 S. G. Kumar and L. G. Devi, *J. Phys. Chem. A*, 2011, **115**, 13211–13241.

14 N. Belachew, M. H. Kahsay, A. Tadesse and K. Basavaiah, *J. Environ. Chem. Eng.*, 2020, **8**, 104106.

15 L. Zhang, H. Fu, C. Zhang and Y. Zhu, *J. Solid State Chem.*, 2006, **179**, 804–811.

16 D. Chen and J. Ye, *Chem. Mater.*, 2009, **21**, 2327–2333.

17 A. Mukherji, B. Seger, G. Q. Lu and L. Wang, *ACS Nano*, 2011, **5**, 3483–3492.

18 H. Xing, H. Ma, Y. Fu, X. Zhang, X. Dong and X. Zhang, *J. Renewable Sustainable Energy*, 2015, **7**, 063120.

19 J. Tang, Z. Zou and J. Ye, *Catal. Lett.*, 2004, **92**, 53–56.

20 L. Zhang, D. Chen and X. Jiao, *J. Phys. Chem. B*, 2006, **110**, 2668–2673.

21 L. Zhang, W. Wang, L. Zhou and H. Xu, *Small*, 2007, **3**, 1618–1625.

22 L. Zhou, W. Wang, H. Xu, S. Sun and M. Shang, *Chemistry*, 2009, **15**, 1776–1782.

23 Z.-Q. Li, X.-T. Chen and Z.-L. Xue, *CrystEngComm*, 2013, **15**, 498–508.

24 Y. Jia, Y. Ma, J. Tang and W. Shi, *Dalton Trans.*, 2018, **47**, 5542–5547.

25 S. Williams, M. Puri, A. J. Jacobson and C. A. Mims, *Catal. Today*, 1997, **37**, 43–49.

26 N. Hykaway, W. M. Sears, R. F. Frindt and S. Roy Morrison, *Sens. Actuators*, 1988, **15**, 105–118.

27 A. Watanabe and H. Kodama, *J. Solid State Chem.*, 1980, **35**, 240–245.

28 R. M. Atlas, *Handbook of Microbiological Media*, CRC Press, 3rd edn, 2004.

29 L. Banavatu, D. S. Rao and K. Basavaiah, *Asian J. Chem.*, 2018, **30**, 97–102.

30 K. Schuh, W. Kleist, M. Høj, V. Trouillet, A. D. Jensen and J.-D. Grunwaldt, *Chem. Commun.*, 2014, **50**, 15404–15406.

31 X. Zhao, T. Xu, W. Yao and Y. Zhu, *Thin Solid Films*, 2009, **517**, 5813–5818.

32 M. T. Le, D. Van Hung, D. D. Truong and N. N. Pham, *J. Chin. Chem. Soc.*, 2017, **64**, 1326–1332.

33 F. D. Hardcastle and I. E. Wachs, *J. Phys. Chem.*, 1991, **95**, 5031–5041.

34 I. D. Brown and K. K. Wu, *Acta Crystallogr., Sect. B: Struct. Crystallogr. Cryst. Chem.*, 1976, **32**, 1957–1959.

35 C. Li, Z. Gao, X. Tian, J. Zhang, D. Ju, Q. Wu, W. Lu, Y. Sun, D. Cui and X. Tao, *CrystEngComm*, 2019, **21**, 2508–2516.

36 F. D. Hardcastle and I. E. Wachs, *J. Phys. Chem.*, 1991, **95**, 10763–10772.

37 J. Zhao and X. Yang, *Building and Environment*, 2003, **38**, 645–654.

38 D. P. Das, N. Biswal, S. Martha and K. M. Parida, *J. Mol. Catal. A: Chem.*, 2011, **349**, 36–41.

39 Y. Yu, C. Li, S. Huang, Z. Hu, Z. Chen and H. Gao, *RSC Adv.*, 2018, **8**, 32368–32376.

40 N. Belachew, D. S. Meshesha and K. Basavaiah, *RSC Adv.*, 2019, **9**, 39264–39271.